Nonlinear oscillations and collapse of elongated bubbles subject to weak viscous effects: Effect of internal overpressure

Kostas Tsiglifis[a] and Nikos A. Pelekasis[b]
Department of Mechanical & Industrial Engineering, University of Thessaly, Volos 38334, Greece

(Received 18 February 2006; accepted 24 May 2007; published online 13 July 2007)

The details of nonlinear oscillations and collapse of elongated bubbles, subject to large internal overpressure, are studied by a boundary integral method. Weak viscous effects on the liquid side are accounted for by integrating the equations of motion across the boundary layer that is formed adjacent to the interface. For relatively large bubbles with initial radius R_0 on the order of millimeters, $P_{St}=P'_{St}/(2\sigma/R_0)\sim 300$ and $\mathrm{Oh}=\mu/(\sigma R_0\rho)^{1/2}\sim 200$, and an almost spherical initial shape, $S\sim 1$, Rayleigh-Taylor instability prevails and the bubble breaks up as a result of growth of higher modes and the development of regions of very small radius of curvature; σ, ρ, μ, and P'_{St} denote the surface tension, density, viscosity, and dimensional static pressure in the host liquid while S is the ratio between the length of the minor semiaxis of the bubble, taken as an axisymmetric ellipsoid, and its equivalent radius R_0. For finite initial elongations, $0.5\leqslant S<1$, the bubble collapses either via two jets that counterpropagate along the axis of symmetry and eventually coalesce at the equatorial plane, or in the form of a sink flow approaching the center of the bubble along the equatorial plane. This pattern persists for the above range of initial elongations examined and large internal overpressure amplitudes, $\varepsilon_B\geqslant 1$, irrespective of Oh. It is largely due to the phase in the growth of the second Legendre mode during the after-bounce of the oscillating bubble, during which it acquires large enough positive accelerations for collapse to take place. For smaller bubbles with initial radius on the order of micrometers, $P_{St}\sim 4$ and $\mathrm{Oh}\sim 20$, and small initial elongations, $0.75<S\leqslant 1$, viscosity counteracts P_2 growth and subsequent jet motion, thus giving rise to a critical value of Oh^{-1} below which the bubble eventually returns to its equilibrium spherical shape, whereas above it collapse via jet impact or sink flow is obtained. For moderate elongations, $0.5\leqslant S\leqslant 0.75$, and large overpressures, $\varepsilon_B\geqslant 0.2$, jet propagation and impact along the axis of symmetry prevails irrespective of Oh. For very large elongations, $S<0.5$, and above a certain threshold value of Oh the counterpropagating jets pinch the contracting bubble sidewalls in an off-centered fashion. © *2007 American Institute of Physics*. [DOI: 10.1063/1.2749421]

I. INTRODUCTION

The fashion by which a bubble collapses has been investigated extensively since Rayleigh's[1] first study on the spherosymmetric collapse of cavitation bubbles in the context of propeller damage. Asymmetric bubble collapse was addressed later on[2,3] in order to assess the destructive effect of jet formation during collapse near a solid boundary. This was facilitated by resorting to the boundary integral formulation that requires discretization of the bubble-liquid interface and the rigid or free boundaries that interact with the bubble, rather than the entire flow domain. This is of course possible in the potential flow regime that is applicable to the case of collapsing bubbles. The destructive effects of the shock wave that is generated by the spherical implosion of a collapsing bubble and of the jet that is formed during asymmetric collapse have been captured and verified experimentally[4,5] with high-speed photography, and they are both known to contribute to plastic deformation of nearby material. Recent advances in computational and cinematographic observation techniques have afforded capturing the details of collapse and in particular the formation of toroidal[6,7] bubbles at jet impact in the presence of a solid boundary.

The details of bubble collapse have recently been singled out as a key factor in the context of single bubble sonoluminescence[8] (SBSL) and single cavitation bubble luminescence[9] (SCBL) experiments, where light is emitted during the final stages of collapse of a bubble that is generated and held captive via acoustic bubble traps or strong laser pulses, respectively. The initial shape of bubbles induced via laser pulses is easier controlled, hence bubbles generated in this fashion are often used as a means to examine the effect of sphericity during collapse on the level of light emission. Thus, it was seen[9] by comparing the collapse of a free bubble against that of a bubble in the vicinity of a solid boundary, via a high speed image converted camera, that in the former arrangement light emission is stronger owing to the higher sphericity of collapse. The pulse duration in these experiments was in the order of a few nanoseconds and the bubbles that were generated had sizes on the order of 1 mm while being more or less spherical. More recently, employment of femtosecond, 10^{-15} s, laser pulses was

[a]Electronic mail: kotsigl@uth.gr
[b]Author to whom correspondence should be addressed. Telephone: 30-24210-74102. Fax: 30-24210-74050. Electronic mail: pel@uth.gr

possible,[10] in which case the bubbles that are generated are much smaller in size, on the order of a few micrometers, with more pronounced asymmetries in their initial geometry, i.e., they exhibited an initial elongation along their axis of symmetry. Such bubbles were observed to collapse asymmetrically in a water solution without any light emission, whereas bubbles produced by the nanosecond laser pulses collapsed in a more or less spherosymmetric fashion[10] and this process was accompanied by strong light emission. A complete simulation of laser-induced bubbles is not possible by examining the equations of motion only, as the phenomenon of SCBL is strongly affected by heat and mass transfer especially when one focuses on the dynamics very close to bubble inception and collapse. Few studies in this direction exist in the literature,[11,12] and clearly more fundamental research is warranted in the way of providing accurate predictions of the temperature field during the final stages of bubble collapse. The present study was motivated by the above experiments and is intended to provide a parametric investigation on the details of bubble collapse for different bubble sizes under conditions of weak or strong elongation and large overpressure, and at shedding some light on the effect of initial degree of sphericity on the mechanics of jet formation and impact during bubble collapse.

In a different context, spark-ignited bubbles[13,14] are studied numerically and experimentally in order to provide insight into the mechanism of noise generation in tip vortex flow in the presence of cavitation. In numerical simulations of spark-ignited bubbles that are allowed to deform in between two vertical plates, elongation and initial overpressure also coexist. The pressure signals during bubble splitting and subsequent jet impact are evaluated and correlated with measured noise. It is of interest to capture the pressure signal during the final stages of collapse of bubbles that are initially elongated and pressurized, in the manner described in the next section, and compare the results with those obtained in the above two references.

The boundary element technique is known to be able to provide the details of bubble collapse in various flow arrangements.[2,3,6,13–18] More recently, the idea of integrating the equations of motion across the boundary layer[19] for drop oscillations with surface tension dominating viscous dissipation [low Ohnesorge number regime, $\mathrm{Oh}=\mu/(\rho R\sigma)^{1/2}$], and obtaining an equation for the evolution of the scalar and vector velocity potentials that is valid on the interface, was applied for the case of an elongated bubble.[20] This is particularly useful for bubbles of relatively smaller size, such as those produced by femtosecond laser pulses, where viscosity provides the dominant dissipation mechanism. In the latter study,[20] henceforth referred to as **I** for brevity, it was seen that, for small internal overpressures, jet formation and impact is present when an elongated bubble collapses in the form of two counterpropagating jets that collide at the equatorial plane forming a tiny microbubble that is surrounded by a larger toroidal one. This collapse mechanism arises below a certain threshold value of Oh, above which the bubble eventually returns to its equilibrium spherical shape. The appearance of toroidal bubbles is indeed a recurring theme in studies of collapsing bubbles,[6,15,17,18,20] but it will be seen here how internal overpressure affects this process since this quantity is a good measure of the initial mechanical energy of bubbles that are generated via laser pulses[9,10] or spark ignition.[13,14]

In Sec. II, a brief account is given of the specific features of the problem treated in the present study, i.e., initial conditions and parameter range, as well as a brief account of the governing equations and of the numerical methodology. In Sec. III, a parametric study is carried out of the process of bubble collapse in the appropriate parameter range determined by initial elongation, internal bubble overpressure, bubble size, and viscosity. Different modes of collapse are obtained and the existence of universalities during pinch-off is investigated. Finally, in Sec. IV, conclusions are drawn based on the results of the present study, which are also compared with the findings of similar studies available in the literature, and directions for future research are outlined.

II. PROBLEM FORMULATION AND SOLUTION METHODOLOGY

A. Governing equations

The problem addressed in the present study is similar to that in **I** except for the initial conditions, where specific attention is placed on the level of initial overpressure inside the elongated bubble,

$$P_G(t=0)=P_G(t=0_-)(1+\varepsilon_B), \tag{1a}$$

$$P_G(t=0_-)-P_{\mathrm{St}}=1; \tag{1b}$$

ε_B denotes the amplitude of the internal overpressure and $P_{\mathrm{St}}=P'_{\mathrm{St}}/(2\sigma/R_0)$ denotes the dimensionless static pressure, but it can also serve as a measure of the bubble size; P'_{St} denotes the dimensional static pressure. In the above equations as well as in the rest of this study, the dimensionless formulation used in **I** is adopted, with surface tension and inertia setting the dominant balance that provides the characteristic time, velocity, and pressure scales; when dimensional variables are introduced they will be denoted by primes. The investigated regime of large internal overpressures is characterized by $\varepsilon_B\sim 1$ or larger. The bubble is assumed to be an ellipsoid initially. The level of elongation is again characterized by parameter $S=a/R_0$ with a and R_0 denoting the length of the smaller semiaxis and the radius of a bubble with the same initial volume, V_0, as the elongated bubble, respectively, Fig. 1,

$$V_0=\frac{4}{3}\pi R_0^3=\frac{4}{3}\pi a^2 c - R_0=\left(\frac{3V_0}{4\pi}\right)^{1/3}, \quad \frac{c}{R_0}=\frac{1}{(a/R)^2}=\frac{1}{S^2}. \tag{2}$$

c is the length of the larger semiaxis of the ellipsoid representing the initial shape of the elongated bubble, which assumes the following dimensionless form in spherical coordinates:

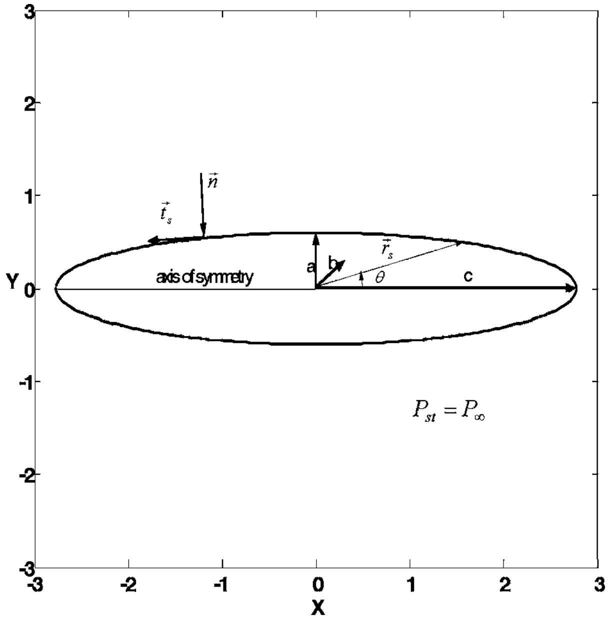

FIG. 1. Schematic diagram of an elongated bubble with initial overpressure.

$$r = f(\theta, t=0) = \frac{S}{\sqrt{S^6 \cos^2\theta + \sin^2\theta}}. \tag{3}$$

As the negative deviation between S and unity increases, $S \leqslant 1$, then the initial elongation of the bubble is intensified. Based on the bubble sizes generated by nanosecond and femtosecond laser pulses in water, the cases with $R=420$ and 5.8 μm are considered, corresponding to a dimensionless static pressure $P_{\mathrm{St}}=295$ and 4.1, respectively. For bubbles of this size in water, $\mathrm{Oh}^{-1}=(\rho R_0 \sigma)^{1/2}/\mu$ is 174 and 20, respectively; σ, ρ, and μ denote surface tension, density, and viscosity in the host liquid. However, for completeness, the parametric study is contacted in S, ε_B, and Oh, with the understanding that the analysis is strictly valid when $\mathrm{Oh}^{-1} \gg 1$, i.e., when viscous forces are less important than surface tension. In this fashion, the problem formulation reads as follows. Lagrangian particles are employed for updating the location of the interface,

$$\frac{dr}{dt} = \frac{(u_n + U_n) r\theta_s + u_t r_s}{\sqrt{r_s^2 + r^2\theta_s^2}}, \tag{4a}$$

$$\frac{d\theta}{dt} = \frac{u_t \mathrm{r}\theta_s - (u_n + U_n) r_s}{r\sqrt{r_s^2 + r^2\theta_s^2}}, \tag{4b}$$

where r, θ, denote the radial and polar spherical coordinates, subscript s denotes partial differentiation with respect to the arc-length s of the generating curve of the axisymmetric interface, t and n are the tangential and normal components of the potential, $\vec{u}=\vec{\nabla}\Phi$, and vortical, $\vec{U}=\vec{\nabla}\times\vec{A}$, part of the fluid velocity and $d/dt=\partial/\partial t+(\vec{u}+U_n\vec{n})\cdot\vec{\nabla}$; $\Phi, \vec{A}$, denote the scalar and vector potentials associated with the fluid velocity. Combining the Bernoulli equation with the normal force balance on the interface, we obtain an equation describing the time evolution of scalar potential on the interface,

$$\frac{d\Phi}{dt} = \frac{u^2}{2} + u_n U_n + 2P_\infty - 2P_G + 2A(\vec{t}\cdot\vec{\nabla}\vec{u}\cdot\vec{n}) - 2H - 2\mathrm{Oh}(\vec{n}\cdot\vec{\nabla}\vec{u}\cdot\vec{n}) \tag{5}$$

that also contains O (Oh) corrections for the normal viscous stress and the vortical part of the pressure on the interface. The normal component, $u_n=\partial\Phi/\partial n$, of the potential velocity field is obtained by recasting the Laplacian in the form of an integral equation evaluated on the interface

$$\Phi(\hat{r},\hat{\theta},t) + \int_0^1 [\Phi(r,\theta,t) - \Phi(\hat{r},\hat{\theta},t)] \times \frac{\partial G}{\partial n}(\hat{r},\hat{\theta},r,\theta) r \sin\theta (r_\xi^2 + r^2\theta_\xi^2)^{1/2} d\xi = \int_0^1 \frac{\partial\Phi}{\partial n}(r,\theta,t) G(\hat{r},\hat{\theta},r,\theta) r \sin\theta (r_\xi^2 + r^2\theta_\xi^2)^{1/2} d\xi, \tag{6}$$

where G and $\partial G/\partial n$ denote the axisymmetric free-space singular kernels of the Laplacian. Owing to axisymmetry, $\vec{A} = A(r,\theta)\vec{e}_\phi$, and integrating the tangential component of the momentum equation across the boundary layer, we obtain an equation describing the time evolution of the vector velocity potential evaluated on the interface,

$$\frac{DA}{Dt} = A(\vec{n}\cdot\vec{\nabla}\vec{u}\cdot\vec{n} - \vec{t}\cdot\vec{\nabla}\vec{u}\cdot\vec{t}) - \mathrm{Oh}\frac{\partial U_t}{\partial n}. \tag{7}$$

Equations (4)–(7), along with the appropriate boundary conditions enforcing axisymmetry at the two poles, provide the description of the bubble dynamics based solely on interfacial variables, including weak viscous effects. For more details on the formulation, the interested reader is referred to Refs. 19 and 20.

As a means to analyze and cross-check the numerical results, the equation describing shape instabilities[12] for an oscillating bubble is employed,

$$\ddot{a}_n + \left[3\frac{\dot{R}}{R} + 2\frac{\mathrm{Oh}}{R^2}(n+2)(2n+1)\right]\dot{a}_n + (n-1)\left[-\frac{\ddot{R}}{R} + \frac{(n+1)(n+2)}{R^2} + 2\frac{\mathrm{Oh}\dot{R}}{R^3}(n+2)\right]a_n, \tag{8}$$

where n denotes the Legendre mode under investigation and $R(t)$ is the time variation of the dimensionless bubble radius as predicted by the Rayleigh-Plesset (RP) equation for an initial disturbance of the form shown in Eq. (1),

$$R\ddot{R} + \frac{3}{2}\dot{R}^2 = 2(P_{\mathrm{St}}+1)(1+\varepsilon_B)R^{-\gamma} - 2P_{\mathrm{St}} - 4\mathrm{Oh}\frac{\dot{R}}{R} - 2. \tag{9}$$

The liquid is treated as incompressible and the gas inside the bubble as ideal with a polytropic constant γ. The above approximation is appropriate since the duration of the investigated phenomena is very short and consequently the boundary layer thickness can be approximated as $\delta' \sim \sqrt{\nu t'}$. Equation (8) is valid provided $\delta' \ll R_0$ or equivalently, $t \ll \mathrm{Oh}^{-1}$, which is indeed the case in the context of the present study.

B. Numerical methodology

The numerical methodology employed for capturing the detailed bubble dynamics is explained in detail in **I**. The kinematic and dynamic boundary conditions, Eqs. (4) and (5), along with the equation describing the evolution of the vector potential, Eq. (7), are discretized via the finite-element method and are integrated in time with the fourth-order accurate Runge-Kutta method. Filtering is applied on the vector potential solution at every time step in order to eliminate short wave instabilities. The normal component of the potential velocity vector is calculated by applying the boundary element method on the integral Eq. (6). In order to accommodate the large initial elongations and overpressures of the bubble as well as the resulting large deformations and jet velocities, use of symmetry is employed, when bubble geometry permits, along with parallel construction of the system matrix that arises as part of the boundary integral methodology. In fact, between 100 and 200 elements are used along half of the generating curve of the interface, $0 \leqslant \theta \leqslant \pi/2$, for moderate initial elongations, $S \geqslant 0.7$, whereas between 300 and 600 elements are used, in the same portion of the θ space, when the initial elongation becomes very large, $S \leqslant 0.6$. Finally, marker points are redistributed at every time step in order to properly resolve areas of high curvature. Subsequently, in order to avoid unstable evolution of marker points, the time step is adapted following the $\Delta t \sim \Delta s_{\min}^{5/2}$ rule for cases with explosive and almost spherosymmetric bubble collapse. The latter scaling arises in the context of the Rayleigh-Plesset equation when the velocity of a spherical bubble during collapse is evaluated,[21] $\dot{R} \sim R^{-3/2}$, which as R becomes vanishing small gives $\Delta t \sim \Delta R^{5/2}$. The latter scaling reflects the dominant balance between inertia and the pressure drop between the far field and the bubble interior. When the initial elongation is relatively large and the bubble collapse asymmetric, the $\Delta t \sim \Delta s_{\min}^{3/2}$ time adaptation rule is employed as suggested by the universality law governing most of the collapse phase of such bubbles, already discussed in **I** and observed in the present study also.

III. PARAMETRIC STUDY

In **I**, the dynamic behavior of elongated bubbles was examined with vanishing or small initial overpressure, and the combined effect of initial elongation and viscous dissipation was investigated. It was thus seen that for small elongations, the bubble will eventually return to its equilibrium spherical shape, whereas above a certain level of elongation, S, smaller than, roughly, 0.6 for zero initial overpressure, a threshold value of Oh^{-1} exists above which the bubble eventually collapses via jet impact giving rise to a toroidal bubble surrounding a tiny microbubble that occupies the central region of the original bubble. The existence of a small initial overpressure does not significantly change this picture, stabilizing the bubble by increasing the critical Oh^{-1} number for jet impact. Overpressure essentially delays the process of jet formation by uniformly expanding the bubble, thus giving more time for viscosity to act and prevent impact. Large internal overpressures are expected to enrich the above dynamic pattern by adding large amounts of energy to the system that may then be converted to inertia with interesting consequences on the bubble dynamics. In this section, the effect of large internal overpressure on the dynamics of micrometer- and millimeter-sized bubbles is investigated as a function of ε_B, S, and Oh. These are very small bubbles and we expect viscous damping to be the dominant dissipation mechanism. In order to assist the analysis of the bubble behavior, the formulas providing the resonance frequencies for volume and shape oscillations, as predicted by linear theory excluding any damping mechanism, are reproduced below,

$$\omega_0 = [6(P_{\mathrm{St}}+1)\gamma - 2]^{1/2} \omega_k = [(k^2-1)(k+2)]^{1/2}, \quad k \geqslant 1. \tag{10}$$

A. Micrometer-sized bubbles, $P_{\mathrm{St}} \sim 4$, $\mathrm{Oh}^{-1} \sim 20$

We first consider bubbles with initial volume characterized by an indicative equivalent radius of 5.8 μm, generated in water at normal conditions, 20 °C and 1 bar, in which case $P_{\mathrm{St}} \approx 4.1$. For bubbles of this size oscillating in water, $\mathrm{Oh}^{-1} \approx 20$. Nevertheless, a parametric study was conducted by varying Oh, in order to capture the effect of viscous dissipation on the breakup mechanism. We consider initial overpressure levels that are characterized by values of ε_B on the order of 1 or larger. In particular, the case with $\varepsilon_B = 2$ was examined for a wide range of initial elongations and viscous dissipation levels. For small initial elongations, $S \geqslant 0.7$, typically between 100 and 200 elements were used in the half theta space and the dimensionless time step varied within one calculation between 5×10^{-4} and 10^{-5}. For large initial elongations, $S \approx 0.45$, typically 350 elements were used in the half theta space and the dimensionless time step varied within one calculation between 10^{-5} and 5×10^{-6}.

When the initial elongation is negligible, $S \sim 1$, the bubble performs a number of volume oscillations during which it gradually becomes more and more deformed due to the onset of higher nonspherical harmonics. Eventually, it settles to its equilibrium spherical shape under the action of viscous dissipation, Fig. 2. Plotting the shape mode decomposition as a function of time indicates gradual decay, and this is corroborated by stability analysis, via Eqs. (8) and (9), of the second spherical harmonic, i.e., the second Legendre polynomial (P_2) in the context of axisymmetric disturbances; see also Figs. 2(b) and 2(c). When the effect of viscous dissipation is mitigated, larger Oh^{-1}, while the rest of the problem parameters remain the same, the time required for returning to the spherosymmetric configuration is longer, until a threshold value of Oh^{-1} is reached above which the bubble pinches off via jet formation and impact in the manner described in **I** for small overpressures; see Figs. 3(a) and 3(b) for the case with $\mathrm{Oh}^{-1} = 40$. The mode decomposition is also depicted as obtained from the numerically calculated bubble shape as well as the stability analysis, Figs. 3(c) and 3(d). In both figures, P_2 exhibits gradual growth during the collapse

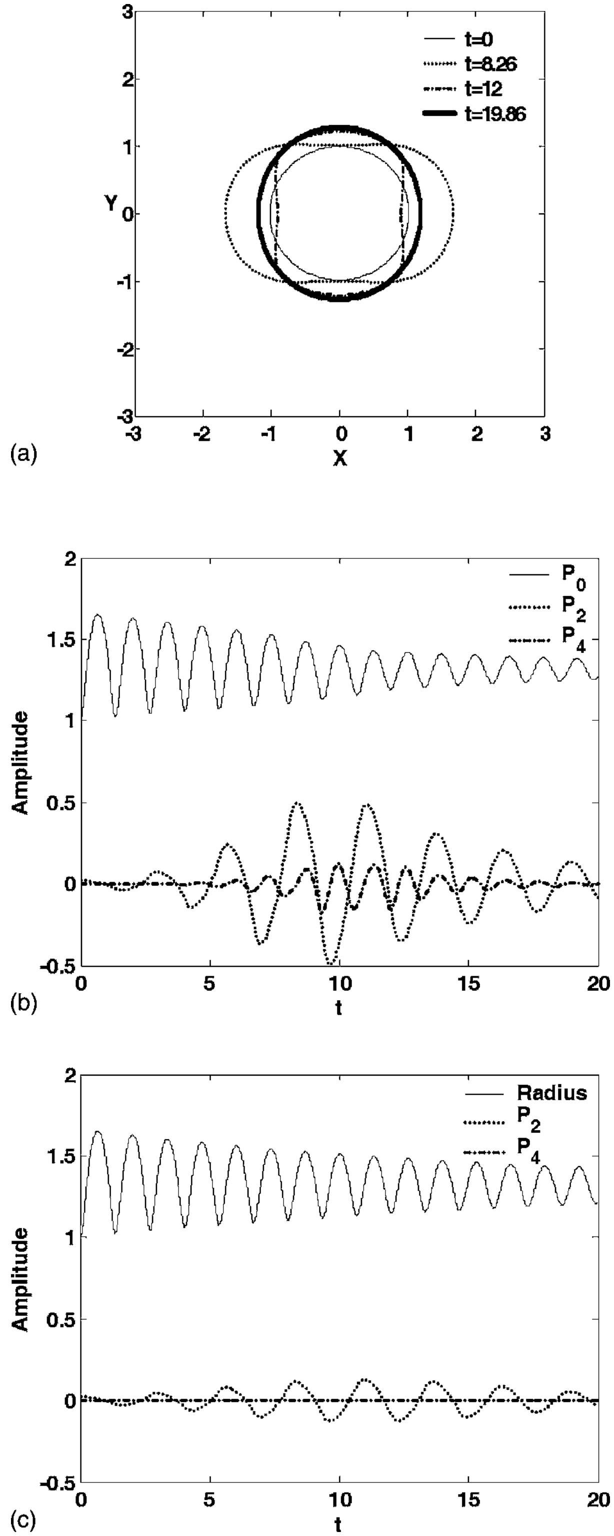

FIG. 2. Time evolution of (a) bubble shapes, (b) numerically obtained shape mode decomposition, and (c) evolution of bubble radius and shape mode decomposition based on stability analysis; $S=0.99$, $P_{\mathrm{St}}=4.1$, $\varepsilon_B=2$, $\mathrm{Oh}^{-1}=20$, with 100 elements in the region $0 \leqslant \theta \leqslant \pi/2$.

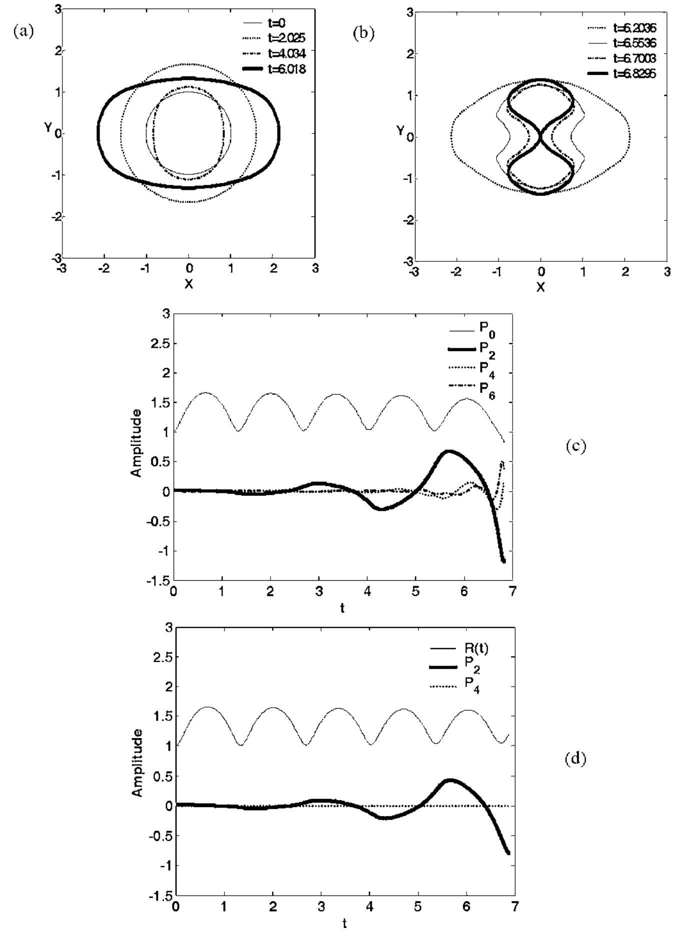

FIG. 3. Time evolution of (a) bubble shapes in the beginning of the motion, (b) bubble shapes during collapse, (c) numerically obtained shape mode decomposition, and (d) evolution of bubble radius and shape mode decomposition based on stability analysis; $S=0.99$, $P_{\mathrm{St}}=4.1$, $\varepsilon_B=2$, $\mathrm{Oh}^{-1}=40$, with 150 elements in the region $0 \leqslant \theta \leqslant \pi/2$.

phase of volume pulsations indicating the onset of an afterbounce instability.[12] The latter is similar to the Rayleigh-Taylor instability since it is also associated with positive gas accelerations during bubble collapse, however it is not as explosive, and the parametric instability since it also exhibits gradual growth, however it does not require as many cycles to appear. It should also be stressed that, based on Eq. (10), $\omega_0 \approx 6.4$, which is almost twice the resonance frequency of P_2, $\omega_2 \approx 3.4$, indicating the possibility for parametric excitation.

When the initial overpressure increases, $\varepsilon_B=10$, the threshold in Oh^{-1} for jet impact decreases also, due to faster growth of P_2, until it covers almost the entire range of Oh number. The rest of the even Legendre modes are either stable or grow but not as fast as P_2, which dominates the dynamics. It is important to note that when the internal overpressure is small or absent,[20] jet formation and impact are heavily dependent on the inertia imparted to the bubble poles due to the initial elongation. As ε_B increases significantly, in contrast to the situation with small initial overpressure ($\varepsilon_B \ll 1$) in which case collapse via jet impact is stabilized, this process is assisted by P_2 growth as a result of the afterbounce instability that allows for jet impact even at very low initial elongations, $S=0.99$, provided viscous damping is not strong enough to eventually overwhelm shape instability. The fashion by which jet impact takes place depends on the phase in the P_2 growth pattern for which its amplitude is large enough for impact to take place. When the amplitude of

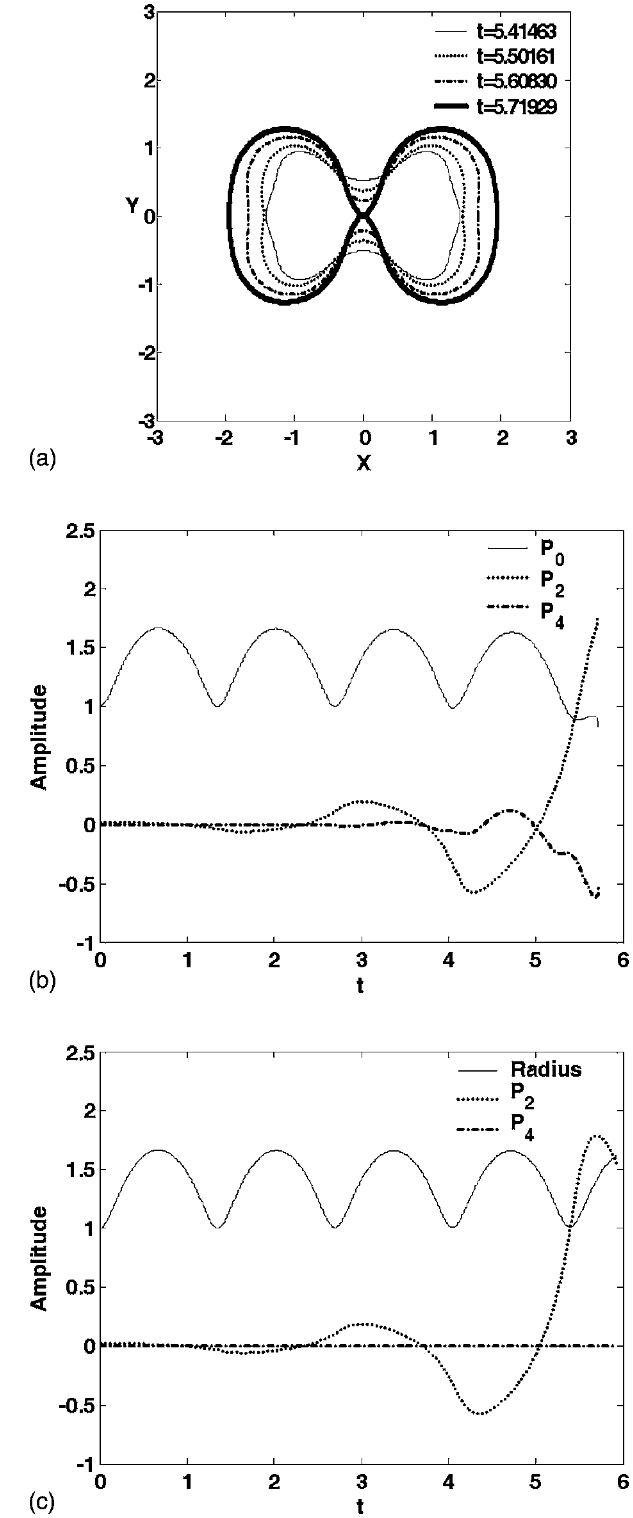

FIG. 4. Time evolution of (a) bubble shapes during collapse, (b) numerically obtained shape mode decomposition, and (c) evolution of bubble radius and shape mode decomposition based on stability analysis; $S=0.99$, $P_{\mathrm{St}}=4.1$, $\varepsilon_B=2$, $\mathrm{Oh}^{-1}=200$, with 150 elements in the region $0 \leqslant \theta \leqslant \pi/2$.

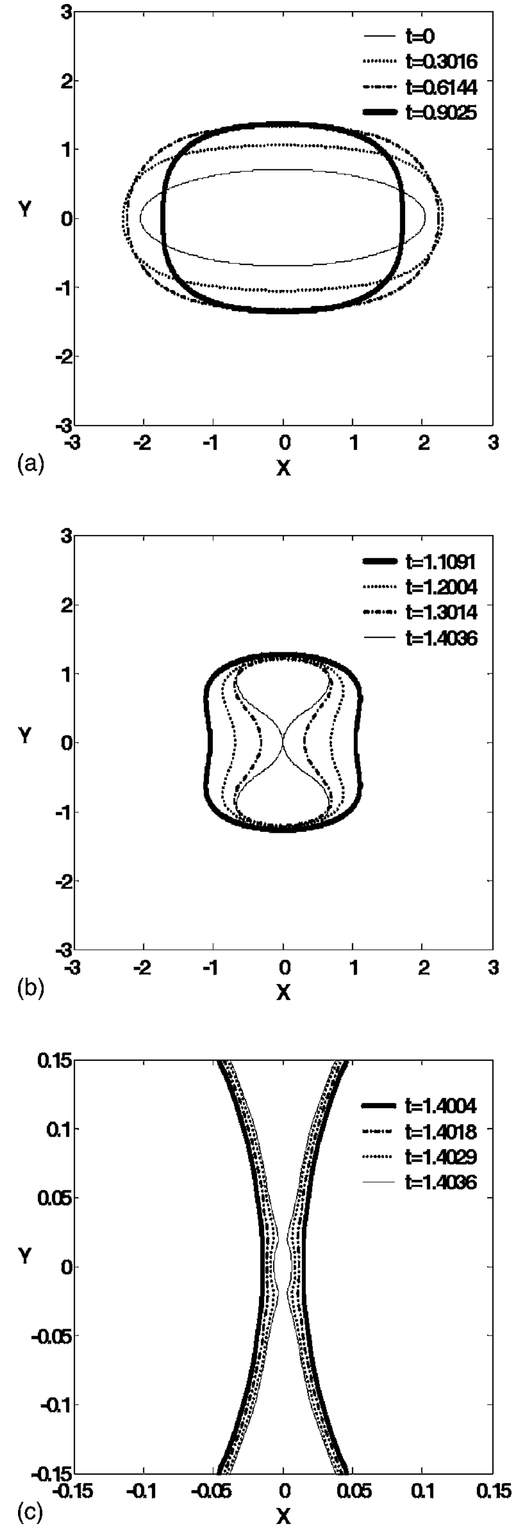

FIG. 5. Time evolution of the shape of the bubble (a) in the beginning of the motion, (b) during jet formation, and (c) during collapse; $S=0.7$, $P_{\mathrm{St}}=4.1$, $\varepsilon_B=2$, $\mathrm{Oh}^{-1}=20$, with 200 elements in the region $0 \leqslant \theta \leqslant \pi/2$.

P_2 grows in time, it does so in the manner shown in Fig. 3, gaining in size during each collapse phase of the pulsating bubble while exhibiting alternating sign with increasing number of pulsation cycles. Thus, when collapse occurs during the positive phase in the P_2 growth cycle, it manifests itself in the form of a sink flow along the equatorial plane that is directed toward the center of the bubble on the axis symmetry. Figure 4 illustrates this behavior when $\mathrm{Oh}^{-1}=200$. When the opposite happens, negative P_2 amplitudes, the jets propagate along the axis of symmetry and coalesce on the equator. The latter is the type of behavior that we obtain in **I** as well as in most cases presented in this study for

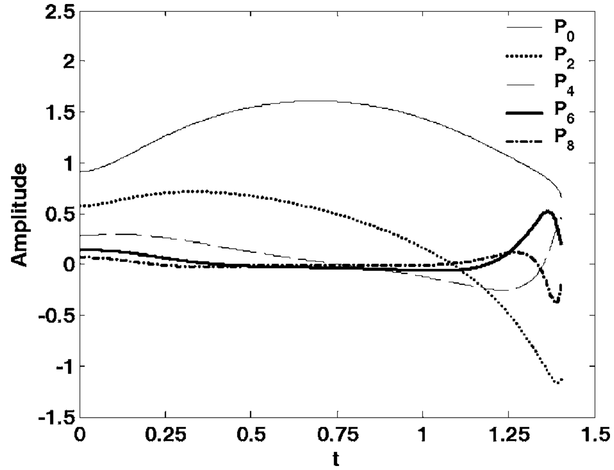

FIG. 6. Time evolution of the numerically obtained shape mode decomposition when $\mathrm{Oh}^{-1}=20$, $S=0.7$, $P_{\mathrm{St}}=4.1$, $\varepsilon_B=2$.

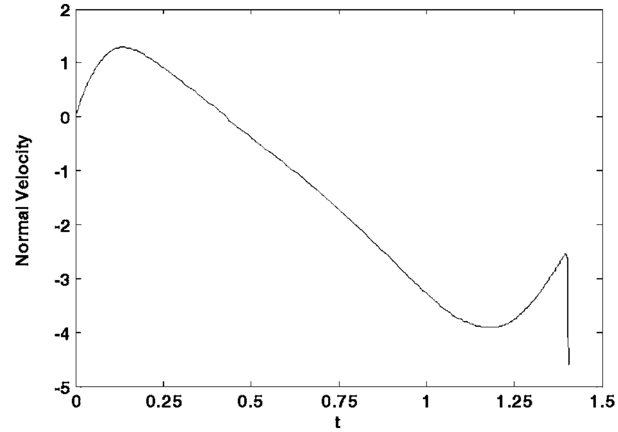

FIG. 7. Time evolution of the dimensional normal velocity of the bubble tip when $\mathrm{Oh}^{-1}=20$ $S=0.7$, $P_{\mathrm{St}}=4.1$, $\varepsilon_B=2$.

relatively large elongations, in which case the initial content of P_2 in the bubble shape is quite substantial, prolate, so that when the shape of the bubble becomes oblate, negative P_2 content, for the first time the propagating jets are fast enough to cause impact. The former type of collapse leads to a different final topology that consists of two larger bubbles and a tiny one occupying the center of the original bubble, i.e., it is not associated with the formation of a toroidal bubble. A collapse mode of this type was also obtained in the context of bubble interaction with a tip vortex or plane boundaries.[13,14] In the latter two studies, the original bubble is seen to collapse on the axis of symmetry before it splits to form two smaller bubbles, which then collapse on their own. The simulations indicate a strong pressure signal in the host liquid in the vicinity of the bubble during the primary collapse followed by a stronger signal during the collapse of the smaller bubbles. The first signal was thought to be an artifact of the numerical process of splitting the bubble. However, its presence is corroborated by the simulations presented here, showing locally a peak pressure accompanying dimple formation during collapse.

As the initial elongation increases, the centered collapse mode via jet impact persists until it occupies the entire range of Oh, $0.5 \leqslant S \leqslant 0.75$, when $\varepsilon_B \geqslant 2$. Within this range of elongations, the bubble always collapses with the two jets coalescing at the equatorial plain irrespective of Oh; see Fig. 5 for $S=0.7$ and $\mathrm{Oh}^{-1}=20$, with the understanding that as Oh increases, the onset of collapse is decelerated. The shape mode decomposition, Fig. 6, confirms the above described pattern of P_2 growth. The evolution of the dimensionless speed of the two bubble tips for the case shown in Fig. 5 is illustrated in Fig. 7 as an indicator of jet velocity. In it as well as in subsequent graphs, negative values of interfacial speed denote inward motion. Initially the bubble tips coincide with the poles. However, during the collapse phase the velocity of the dimple that is formed is shown, hence the slight jump in the curve toward the last stages of jet coalescence. When dimensional quantities are used, jet speeds on the order of 15 m/s are captured, indicating the level of severity during impact. It should be noted that larger jet speeds are developed as Oh^{-1} increases, which, nonetheless, remain of the same order of magnitude. The universal law relating the time from collapse with the 3/2 power of the minimum distance between the two coalescing jets, reported in **I** but also in previous studies of capillary drop pinch-off[22] and attributed to the inertia versus capillarity balance, is seen to hold in the case of large overpressures also, Fig. 8, especially as Oh^{-1} tends to infinity. It should be noted that, based on the above scaling, during the collapse phase the dimple velocity grows like $(t_0-t)^{-1/3}$, where t_0 denotes the time instant at which the approaching dimples meet at the equatorial plane, irrespective of Oh as long as Oh^{-1} remains large. Hence the steep rise in the absolute value of the calculated velocities exhibited toward the very last moments of the collapse phase. The same pattern is recovered in the case of collapse via sink flow along the equatorial plane.

When S becomes smaller than a threshold value, $S_{\mathrm{Cr}} \approx 0.45$ when $\varepsilon_B \geqslant 2$, an additional breakup mechanism arises that evolves in an off-centered fashion. This is illustrated in Figs. 9 and 10, showing the breakup process of an elongated bubble with Oh^{-1} set to 20 and 1000, respectively. In the

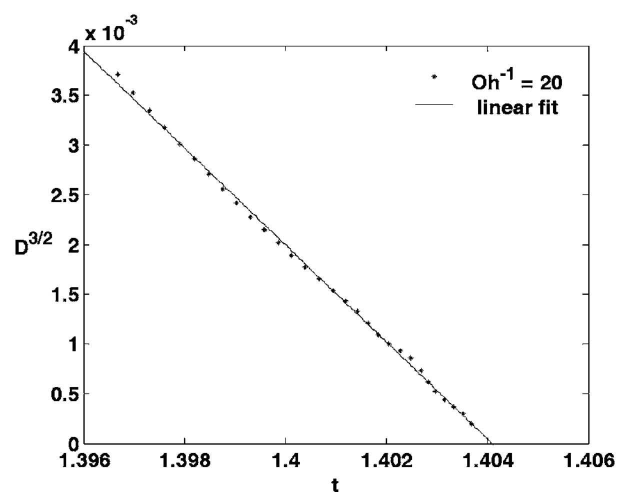

FIG. 8. Time evolution of the distance D, raised to the 3/2 power, between the dimples that are formed on counterpropagating jets when $\mathrm{Oh}^{-1}=20$; $\varepsilon_B=2$ and $S=0.7$.

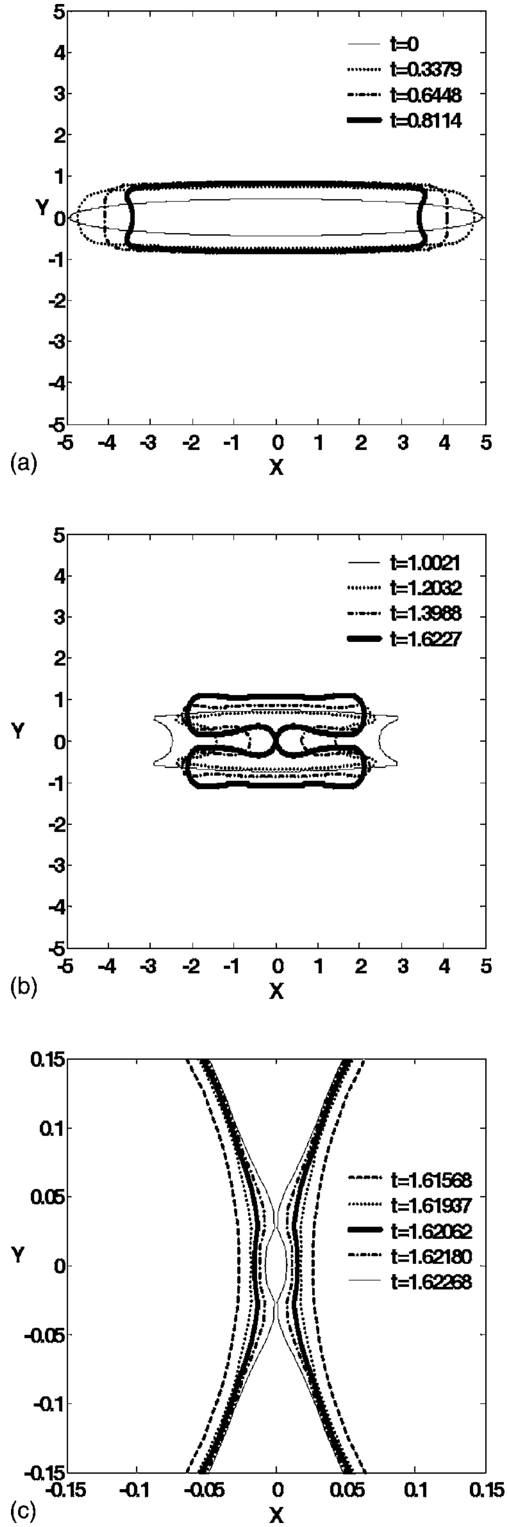

FIG. 9. Time evolution of the shape of the bubble (a) in the beginning of the motion, (b) during jet formation, and (c) during collapse; $S=0.45$, $P_{\mathrm{St}}=4.1$, $\varepsilon_B=2$, $\mathrm{Oh}^{-1}=20$, with 350 elements in the region $0\leqslant\theta\leqslant\pi/2$.

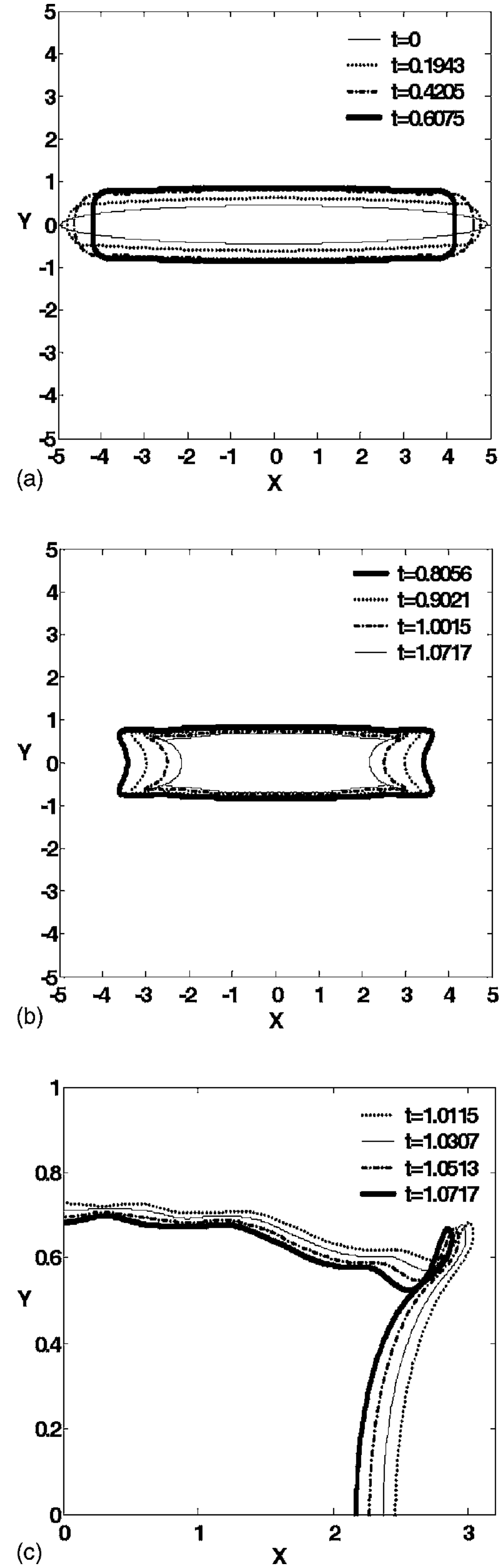

FIG. 10. Time evolution of the shape of the bubble (a) in the beginning of the motion, (b) during jet formation, and (c) during collapse; $S=0.45$, $P_{\mathrm{St}}=4.1$, $\varepsilon_B=2$, $\mathrm{Oh}^{-1}=1000$, with 350 elements in the region $0\leqslant\theta\leqslant\pi/2$.

former case, the centered breakup mechanism reported in **I** and recovered here for smaller elongations, i.e., the one leading to a microbubble and a toroidal bubble, is reproduced. On the other hand, as Oh^{-1} increases, the velocity of the two jets is so large that they penetrate well into the bubble interior before the contraction phase is over. In this process, the portion of the bubble sidewalls that lies closer to the tip that is formed at each one of the two poles approaches the axis of symmetry with a considerable speed. Thus, the bubble sidewalls are close enough to interact with the penetrating jet,

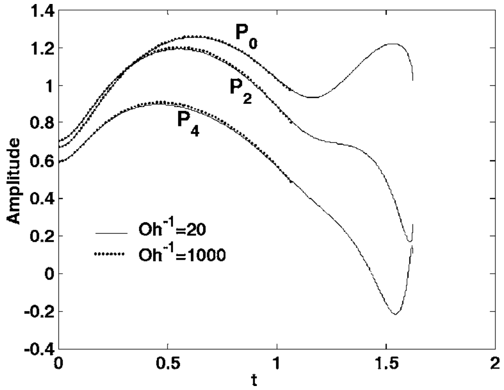

FIG. 11. Time evolution of the numerically obtained shape mode decomposition when $S=0.45$, $P_{\mathrm{St}}=4.1$, $\varepsilon_B=2$, and $\mathrm{Oh}^{-1}=20$ and 1000.

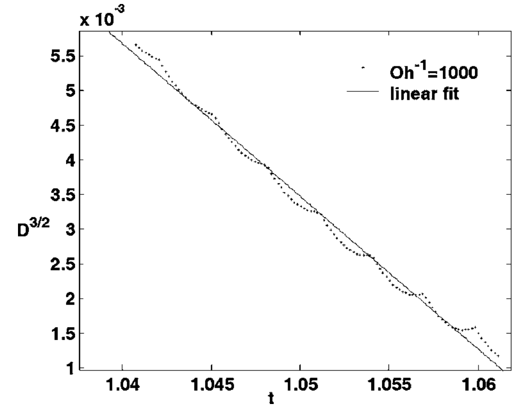

FIG. 12. Time evolution of the distance D, raised to the 3/2 power, between the dimples that are formed on counterpropagating jets when $\mathrm{Oh}^{-1}=1000$; $\varepsilon_B=2$ and $S=0.45$.

eventually leading to an off-centered pinching mechanism. Consequently, instead of proceeding along the axis of symmetry, each one of the two jets pinches at the bubble sidewall giving rise to two smaller toroidal bubbles located in the vicinity of each one of the poles of the original bubble, and a larger bubble occupying the central region of the original bubble.

This is a result of the fact that both P_0 and P_2 are present to a large extent in the bubble dynamics for this parameter range, with P_2 more or less following P_0; see also Fig. 11, illustrating the time evolution of the shape mode decomposition for the above two cases. Thus, as P_0 completes one cycle of its pulsation contracting to its minimum size, P_2 completes half of its own oscillation switching from the initial prolate shape to an oblate one. As a result of synchronization, the two jets penetrating the bubble from each one of the two poles meet the contracting bubble sidewalls. Consequently, each jet faces an increasing bubble pressure and its front becomes more rounded in order to adjust to changes in the pressure difference across the interface. For bubbles of this size, surface tension can accommodate this process and in this fashion the jet front interacts closely with the bubble side walls producing the off-centered collapse mode. When Oh^{-1} decreases, the jets are delayed in penetrating the bubble. Consequently, there is not enough time for them to interact with the bubble walls, hence the centered collapse mode. Similarly as S decreases further, i.e., the bubble is more elongated initially, the jet is faster and the threshold value $\mathrm{Oh}_{\mathrm{Cr}}^{-1}$ for the centered mode to occur decreases. To the extent that the two modes are not significantly detuned, this pattern persists. In fact, increasing ε_B increases the period of P_0, albeit not significantly, and does not affect $\mathrm{Oh}_{\mathrm{Cr}}^{-1}$, which remains as predicted when $\varepsilon_B=2$, $\mathrm{Oh}_{\mathrm{Cr}}\approx 200$.

Monitoring the minimum distance between the jet tip and the bubble sidewall, we can reproduce the universality law mentioned above relating the time from pinch-off with the 3/2 power of the minimum distance, Fig. 12. This result was, to a certain extent, expected since here also the collapsing process involves an inertia versus capillarity balance that is characterized by the above power law. Another interesting aspect of the collapse process is the evolution of the jet speed from inception until collapse and it is depicted in Fig. 13 when $\mathrm{Oh}^{-1}=20$ and 1000. This is a useful quantity if one wants to establish the importance of jet formation in various phenomena such as cavitation damage or even light emission during collapse. As discussed in the Introduction, in both phenomena it is believed that shock wave and jet formation play a role the extent of which, however, in different flow arrangements is not always clear and simulations such as the

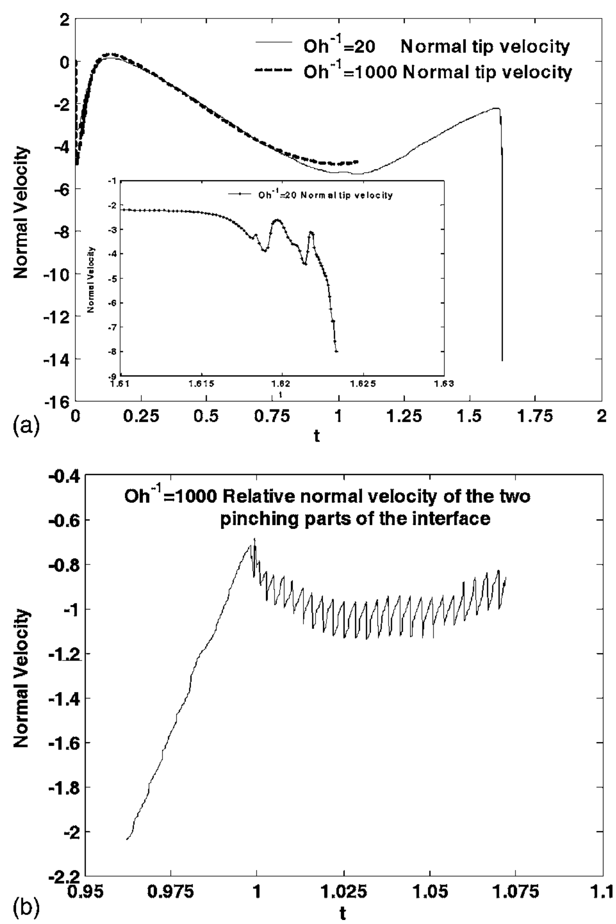

FIG. 13. Time evolution of the dimensionless (a) normal velocity of the bubble tip when $\mathrm{Oh}^{-1}=20$ and 1000 and (b) relative normal velocity of the pinching parts of the bubble's interface when $\mathrm{Oh}^{-1}=1000$; $S=0.45$, $P_{\mathrm{St}}=4.1$, $\varepsilon_B=2$.

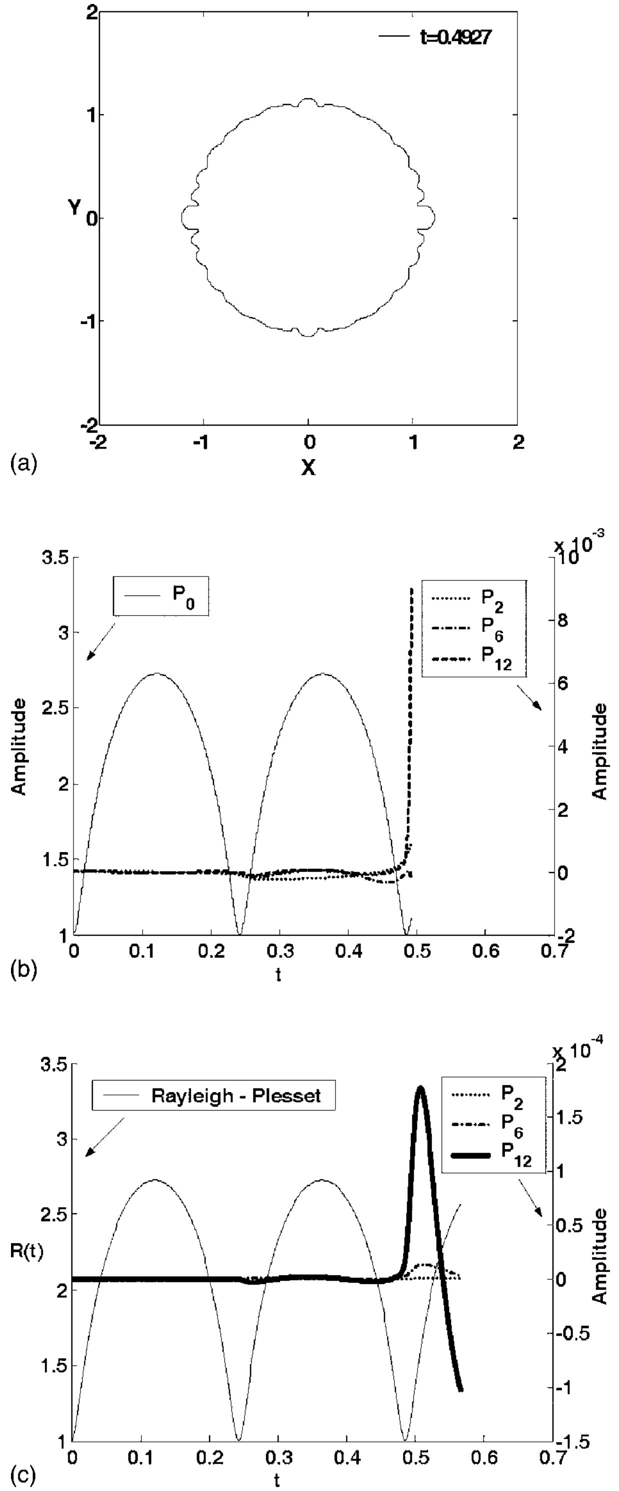

FIG. 14. (a) Bubble shape during collapse, and time evolution of (b) numerically obtained shape mode decomposition and (c) evolution of bubble radius and shape mode decomposition based on stability analysis; $S=1$, $P_{\mathrm{St}}=295$, $\varepsilon_B=10$, $\mathrm{Oh}^{-1}=174$, with 300 elements in the region $0 \leq \theta \leq \pi/2$.

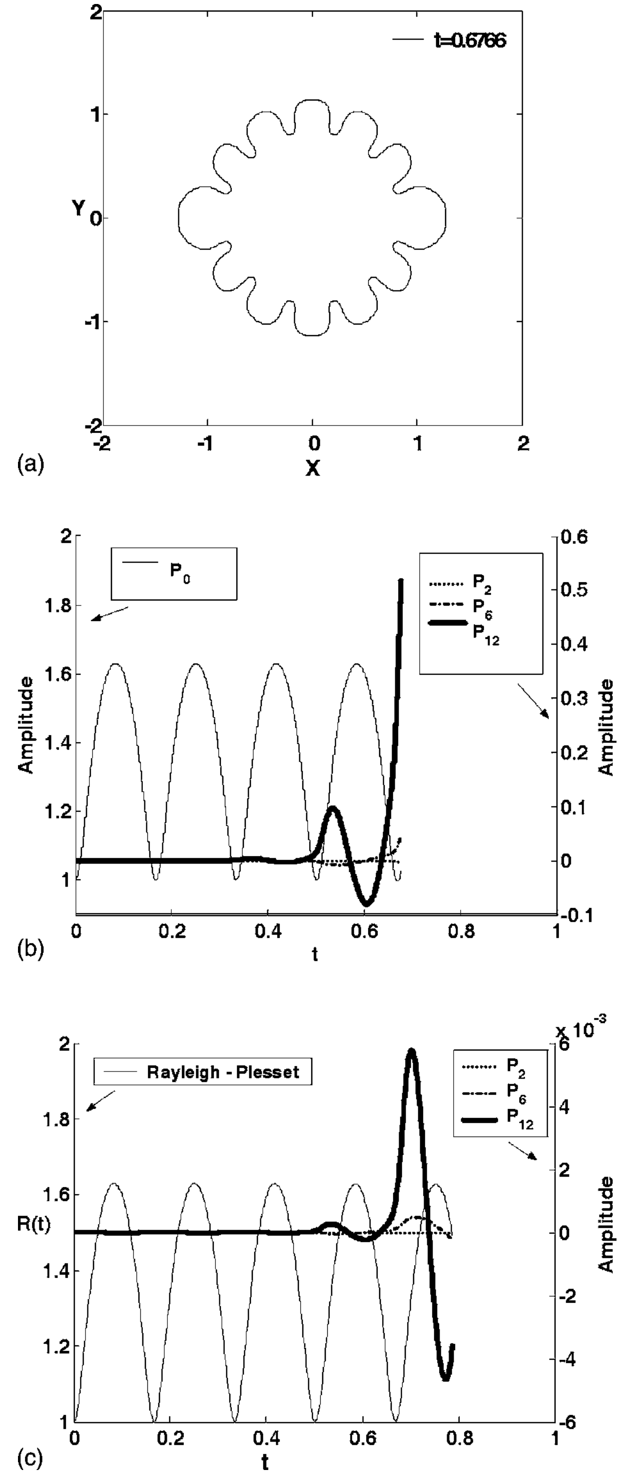

FIG. 15. (a) Bubble shape during collapse, and time evolution of (b) numerically obtained shape mode decomposition and (c) evolution of bubble radius and shape mode decomposition based on stability analysis; $S=1$, $P_{\mathrm{St}}=295$, $\varepsilon_B=2$, $\mathrm{Oh}^{-1}=174$, with 200 elements in the region $0 \leq \theta \leq \pi/2$.

ones presented here can help, along with properly designed experimental investigations, in addressing this issue. The asymptotic increase of jet speed during impact that was discussed in the context of Fig. 7 is also illustrated here in the small inset of Fig. 13(a). Upon comparing the two figures for the case with $\mathrm{Oh}^{-1}=20$, it is concluded that, despite the much larger initial elongation in Fig. 13(a), the jet speed is not significantly increased during collapse. In Fig. 13(b), the relative velocity of the two pinching parts of the interface is shown. It exhibits an oscillatory behavior, without the steep increase in absolute value during the collapse phase. This is due to the fact that the normal velocities of the pinching parts of the interface are not aligned with the line connecting

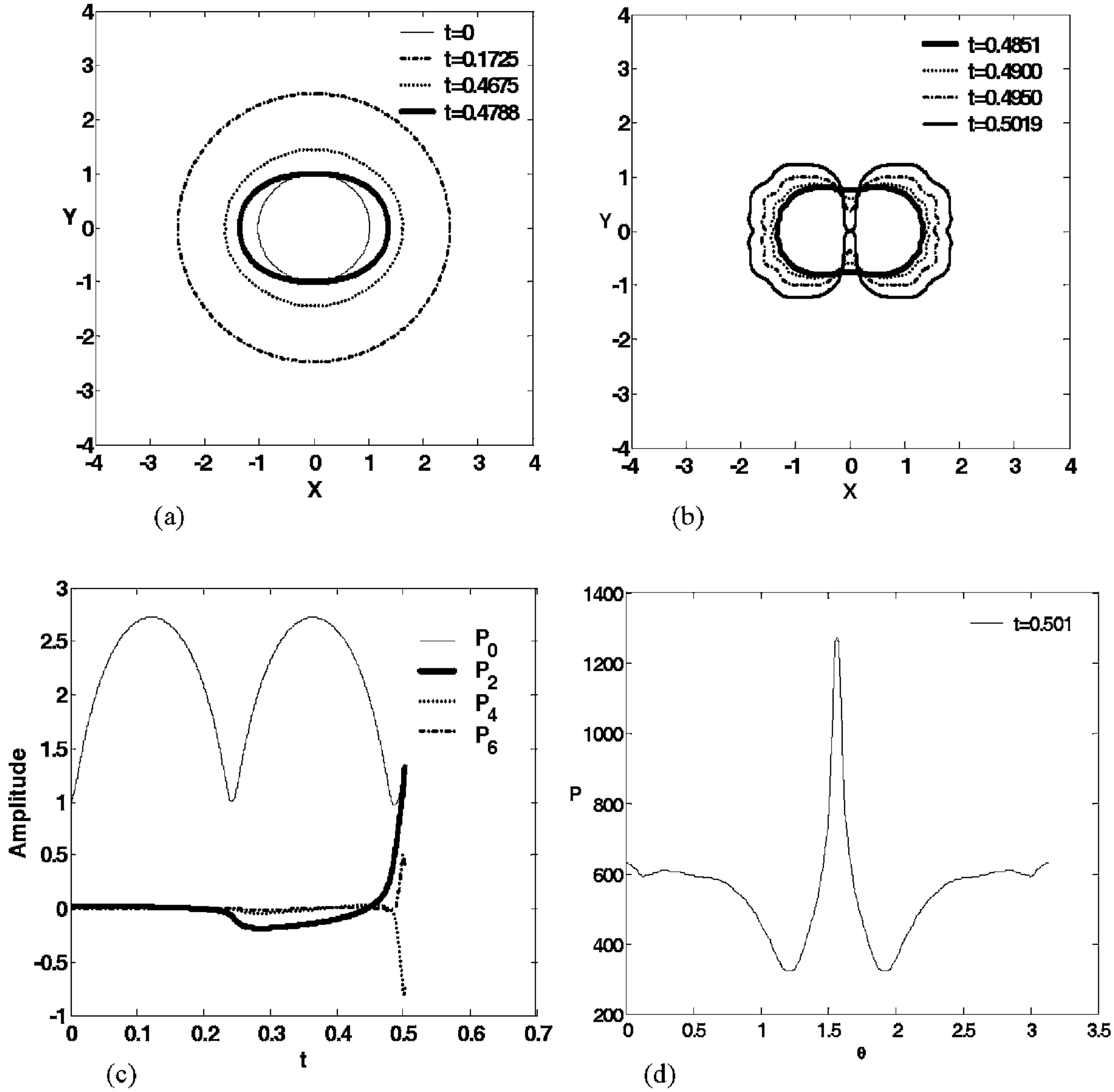

FIG. 16. Time evolution of (a) bubble shapes in the beginning of the motion, (b) bubble shapes during collapse, (c) numerically obtained shape mode decomposition, and (d) dimensionless pressure distribution on the liquid side along the bubble interface at the time instant of impact; $S=0.99$, $P_{\mathrm{St}}=295$, $\varepsilon_B=10$, $\mathrm{Oh}^{-1}=174$, with 200 elements in the region $0 \leqslant \theta \leqslant \pi/2$.

them, as was more or less the case with the centered collapse mode. Nevertheless, the universality law still holds during collapse, Fig. 12, since this is also determined by the balance between inertia and capillarity. In order to compare jet speed from the above calculations and those presented in the following sections, the speed of the pole at the instant of dimple formation is used as an indicative jet speed. From this point on, the universality law takes over leading to increasingly large dimple velocities until collapse.

Simulations with the bubble oscillations treated as isothermal were also carried out. In this case, part of the energy of the system is consumed in order to maintain the bubble at a constant temperature and this has the same effect as a small reduction of Oh^{-1}, favoring the centered collapse mode. In other words, the rest of the problem parameters remaining fixed, the critical Oh^{-1} value for the collapse process to switch from the centered to the off-centered mode increases, with respect to the threshold value for adiabatic oscillations. The rest of the details of collapse do not change significantly when isothermal conditions are assumed, except for the time to collapse which is longer.

B. Millimeter-sized bubbles, $P_{\mathrm{St}}\sim 300$, $\mathrm{Oh}^{-1}\sim 180$

The collapse mode of bubbles of larger size was also examined, with a characteristic radius $R=420\ \mu\mathrm{m}$, for large initial overpressures and over a range of elongations. Owing to the large size of such bubbles, $P_{\mathrm{St}}=295$ and $\mathrm{Oh}^{-1}=174$ for air bubbles oscillating in water at atmospheric pressure, and consequently viscous dissipation does not play as important a role in the system dynamics as was the case with the micrometer-sized bubbles examined in Sec. III A. In fact, simulations with Oh^{-1} ranging from 20 to infinity were carried out and no significant effect on the collapse mode was observed. This is a result of the larger size of the bubble and the resulting domination of inertia effects over dissipation.

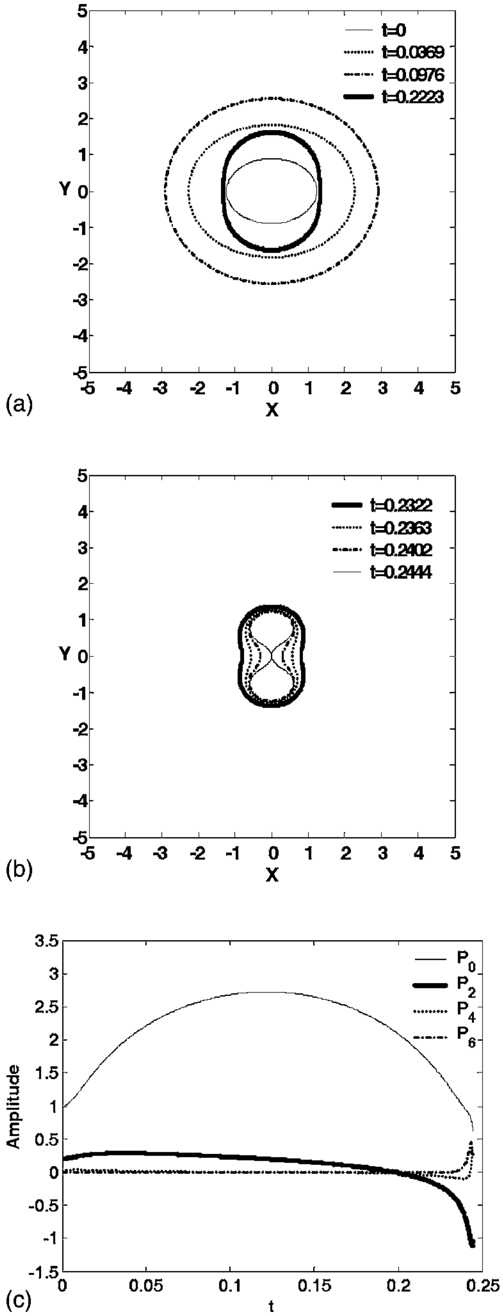

FIG. 17. Time evolution of (a) bubble shapes in the beginning of the motion, (b) bubble shapes during collapse, and (c) numerically obtained shape mode decomposition; $S=0.9$, $P_{\mathrm{St}}=295$, $\varepsilon_B=10$, $\mathrm{Oh}^{-1}=174$, with 200 elements in the region $0\leqslant\theta\leqslant\pi/2$.

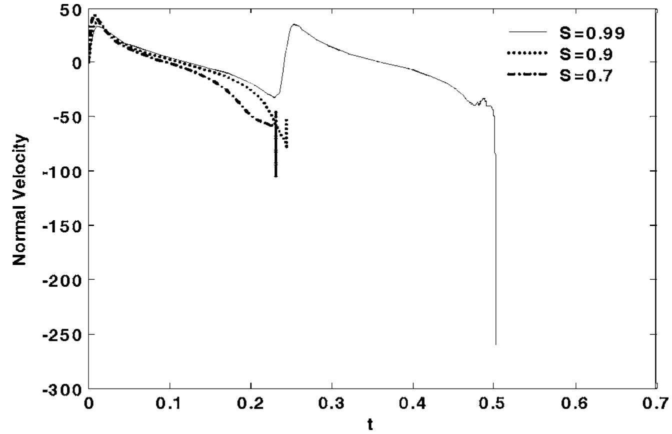

FIG. 18. Time evolution of the dimensionless normal velocity of the bubble tip with increasing initial elongation, $S=0.99$, 0.9, and 0.7; $P_{\mathrm{St}}=295$, $\varepsilon_B=10$, and $\mathrm{Oh}^{-1}=174$.

For small initial elongations, $S\approx 0.99$, typically 200 elements were used in the half theta space and the dimensionless time step varied within one calculation between 10^{-4} and 5×10^{-7} in order to accommodate the explosive collapse phase of the bubble during which $\Delta t\sim\Delta s_{\min}^{5/2}$. For moderate initial elongations, $S\geqslant 0.7$, larger time steps were used ranging from 10^{-5} to 2×10^{-6}. For large initial elongations, $S\approx 0.45$, the number of elements varied during one calculation from 350 to 600 in the half theta space, in order to properly capture the penetrating jets, while the dimensionless time step varied between 10^{-5} and 10^{-6}.

If a perfectly spherical shape is assumed, $S=1$, while maintaining a large initial overpressure, $\varepsilon_B\geqslant 1$, the bubble performs volume oscillations until it eventually breaks up as a result of an explosive Rayleigh-Taylor instability that is expected to destroy its integrity creating fragments of smaller bubbles. Figures 14 and 15 illustrate this behavior in the final bubble shape before collapse and in the time history of the shape mode decomposition as obtained numerically and predicted by linear stability analysis assuming an initial disturbance on the order of the computational accuracy, $a_n(t=0)=10^{-6}$. As can be gleaned from the final shapes and the shape mode decompositions shown in Figs. 14 and 15, higher modes grow very fast leading to a violent bubble collapse via neck formation characterized by local areas of very low curvature. In fact, when $\varepsilon_B=2P_{12}$ grows the fastest, it leads to the formation of 12 satellite bubbles that are expected to eventually fragment the bubble. It is also interesting to note that P_2 is stable when $\varepsilon_B=2$.

For very large initial overpressure, $\varepsilon_B\sim 10$, and finite initial elongation, $S<1$, growth of P_2 is observed in the form of an after-bounce instability that arises during the rebound of the bubble from its minimum volume. The microbubble collapses in a centered fashion, either via a sink flow along the equatorial plane toward the center of the bubble, Fig. 16 for $S=0.99$, or via two jets that propagate in the opposite direction along the axis of symmetry and coalesce at the equatorial plane, Fig. 17 for $S=0.9$. One of the two patterns prevails depending on the phase of P_2 growth during collapse, in the manner described in Sec. III A and verified by the shape mode decomposition shown in Figs. 16(c) and 17(c). When $\varepsilon_B=10$, the latter type of collapse, involving jet propagation along the symmetry axis, is recovered for a wide range of initial elongations, $0.5\leqslant S\leqslant 0.9$. As the initial overpressure increases further, $\varepsilon_B>10$, the same differentiation in the type of collapse is observed, depending on the initial elongation, with the range in S corresponding to sink flow along the equator increasing. In both cases, pinching observes the 3/2 power law during the breakup process.

Experiments[13,14] with spark-ignited bubbles, size on the order of 450 μm, and subject to internal overpressure, indicate collapse on the axis of symmetry and bubble fission.

TABLE I. Collapse pattern for micrometer-sized bubbles depending on the parameter range.

Bubbles with initial radius $R_0 \sim 5$ μm in water at 1 atm; $P_{St} \sim 4$, Oh ~ 20	
Initial elongation S	Type of collapse
Small elongations, $S \sim 1$, e.g., $0.75 < S \leqslant 1$ when $\varepsilon_B = 2$	$\mathrm{Oh}^{-1} > \mathrm{Oh}_{\mathrm{Cr}}^{-1}$ collapse via jet impact along the axis of symmetry or sink flow along the equator due to P_2 growth during the bubble after-bounce, $\mathrm{Oh}^{-1} < \mathrm{Oh}_{\mathrm{Cr}}^{-1}$ damping of oscillations as S decreases or ε_B increases $\mathrm{Oh}_{\mathrm{Cr}}^{-1}$ decreases
Moderate elongations, e.g., $0.5 < S \leqslant 0.75$ when $\varepsilon_B = 2$	Collapse via jet impact along the axis of symmetry irrespective of Oh, as ε_B increases the upper limit of the S interval increases
Large elongations, $S < 0.5$	$\mathrm{Oh}^{-1} < \mathrm{Oh}_{\mathrm{Cr}}^{-1}$, collapse via jet impact along the axis of symmetry, $\mathrm{Oh}^{-1} > \mathrm{Oh}_{\mathrm{Cr}}^{-1}$ off-centered collapse mode, as S decreases $\mathrm{Oh}_{\mathrm{Cr}}^{-1}$ decreases, ε_B does not affect $\mathrm{Oh}_{\mathrm{Cr}}^{-1}(2 \leqslant \varepsilon_B \leqslant 10)$

Simulations were also carried out with the boundary integral method[14] covering a wide parameter range. For bubble sizes on the order of 450 μm, simulations reported in the above study recover the experimentally observed collapse pattern. In addition, they indicate a large pressure signal in the host fluid, at the time that the bubble splits and in the vicinity of the pinching area, which was conjectured to be a numerical artifact. Numerical simulations performed in the context of the present study also reveal that the pressure in the host fluid exhibits a strong peak in the vicinity of the region where impact takes place. Figure 16(b) shows the shape of the bubble during collapse, illustrating the region where the sink flow converges, i.e., around the equator. It is near this region that the liquid pressure peaks, Fig. 16(d), and is expected to emit a strong pressure signal. The latter follows the details of the bubble shape. There is uncertainty regarding the accuracy of the actual numbers, since compressibility is expected to decelerate liquid motion toward the very last stages of collapse, but the strong pressure signal is definitely there. The same was true for small overpressures, as was shown in Fig. 11(e) of **I**, but to a lesser extent. Consequently, the intense pressure signal reported at the moment of bubble fission in Ref. 14 is verified.

A large number of simulations were also conducted with varying Oh number without any effect on the collapse mode. Figure 18 compares dimensionless tip velocities for three different elongations. When $S=0.9$ and 0.7, each tip is located at the poles of the axis of symmetry, whereas when $S=0.99$ the tip is located at the equator. Jet speeds at collapse tend to increase with decreasing initial elongation while they are higher that those calculated for micrometer-sized bubbles, Figs. 7 and 13, indicating the larger effect of final impact for bubbles of this size. In all the above cases, the speed of the approaching tip at the instant of dimple formation was used as an indicative jet speed in the comparison. We use the term jet speed for the case of sink flow as well in order to indicate the localized nature of both types of collapse. When the bubble is almost spherical, $S \geqslant 0.95$, and the initial overpressure not very large, $\varepsilon_B=2$, the bubble collapses after a number of periods of oscillations, in a fashion similar to the situation illustrated in Fig. 15 leading to fragmentation. This is a result of the stability of P_2 for this parameter range and the growth of higher modes that generate areas of very low radius of curvature where rupture is more likely to happen. For larger elongations, $0.5 \leqslant S \leqslant 0.95$, P_2 exhibits growth and the centered collapse mode, involving jet propagation along the axis of symmetry, is recovered for the entire range of S and ε_B values examined. It should be stressed that for S values below 0.45, the off-centered collapse mode prevails, due to the large jet speed that enhances interaction with the sidewalls during the contraction phase. As was explained in the preceding subsection, this leads to rounding of the jet front and pinching at the sidewalls.

IV. CONCLUSIONS

An extensive parametric study was carried out numerically, regarding the collapse mode of small bubbles, initial radius on the order of 6 μm corresponding to $P_{St} \approx 4$ and $\mathrm{Oh}^{-1} \approx 20$, and large bubbles, initial radius on the order of 400 μm corresponding to $P_{St} \approx 300$ and $\mathrm{Oh}^{-1} \approx 180$, in water under atmospheric pressure, subject to large internal overpressures with characteristic amplitude ε_B, and a wide range of initial elongations S. For small bubbles it is seen that for small elongations, $S \sim 1$, and large overpressures, $\varepsilon_B \sim 1$, a threshold value exists in Oh^{-1} above which the bubble collapses via jet formation or sink flow as a result of P_2 growth due to an after-bounce instability, whereas below this threshold it eventually settles to its equilibrium state. Increasing ε_B destabilizes the bubble by decreasing the threshold in Oh^{-1} for P_2 growth. For moderate initial elongations, e.g., $0.5 \leqslant S \leqslant 0.75$ when $\varepsilon_B=2$, and the entire range of initial overpressures that was investigated, $2 \leqslant \varepsilon_B \leqslant 10$, the collapse mode via jet propagation and impact along the axis of symmetry prevails irrespective of Oh, with the upper limit of the S interval increasing as ε_B increases. This is a combined effect of the initial P_2 level and unstable growth. As S is further reduced, $S < 0.5$, an off-centered collapse mechanism arises that involves interaction between the penetrating jets and the contracting bubble sidewalls. The centered collapse mode along the axis of symmetry probably takes place in experiments with asymmetrically collapsing femtosecond laser bubbles,[10] whose size is on the order of a few μm, operating in the very large initial elongation and initial overpres-

TABLE II. Collapse pattern for millimeter-sized bubbles depending on the parameter range.

Bubbles with initial radius $R_0 \sim 400$ μm in water at 1 atm; $P_{St} \sim 300$, Oh ~ 180	
Initial elongation S	Type of collapse
Almost spherical bubble, $S \sim 1, 1 \leqslant \varepsilon_B$	Bubble fissions via Rayleigh-Taylor instability
Very small initial elongation, $0.95 \leqslant S < 1$ for large $\varepsilon_B \geqslant 10$	Collapse via sink flow along the equator as ε_B increases the intensity of impact increases
Large initial elongation $0.5 \leqslant S \leqslant 0.9$, $\varepsilon_B \geqslant 2$	Collapse via jet formation along the axis of symmetry
Very large initial elongation, $S \leqslant 0.45$	Collapse via the off-centered mode

sure parameter range. It should be noted that the available experimental observations could not resolve jet formation and impact due to the angle of observation.

When the parametric study focuses on large bubbles, $P_{St} \sim 300$ and $\text{Oh}^{-1} \sim 200$, the effect of Oh, i.e., viscous dissipation, is minimal. For large internal overpressures, $\varepsilon_B \geqslant 1$, and very small elongations, $S \sim 1$, the bubble breaks up as a result of Rayleigh-Taylor instability. Shape mode decomposition obtained numerically, and corroborated by stability analysis, captures the growth of high axisymmetric modes that leads to satellite bubble formation and breakup in regions of very small radius of curvature. In the presence of small but finite initial elongation, $S < 1$, impact is observed due to growth of P_2 in the form of an after-bounce instability, as also verified by stability analysis. Jet propagation occurs along the axis of symmetry or sink flow takes place along the equator, depending on the phase in P_2 growth. In fact, for very large initial overpressures and very small elongations, $\varepsilon_B \sim 10$ and $S \geqslant 0.95$, propagation along the equator prevails. The latter may take longer to be initiated, due to the small initial P_2 content, but leads to a more explosive impact as a result of the increased sphericity of the bubble. For not very small elongations, $S < 0.9$, jet propagation occurs along the axis of symmetry irrespective of ε_B. In fact, this type of behavior persists for quite large elongations, i.e., S values as small as 0.5, below which the off-centered mode prevails. Collapse via sink flow is probably responsible for the collapse pattern observed in experiments of nanosecond laser bubbles,[10] size on the order of half a millimeter, where the available recordings indicate a similar mode of impact. The above collapse patterns as obtained via the parametric study are schematically shown in Tables I and II.

In the literature,[13,14] bubble pinching in the presence of elongation and overpressure has also been obtained in a different context, when spark-ignited bubbles are allowed to deform between two vertical plates. The two bubble fragments are followed after fission occurs, until reentrant jet formation and impact takes place in the tips corresponding to the north and south poles of the original bubble. The present study also captures sink flow along the equator and pinching on the axis of symmetry while verifying the appearance of a strong pressure signal during this process. The post pinching behavior of the bubble is not captured here. An interesting issue arises regarding the post pinching bubble behavior since experiments with collapsing laser bubbles, which are also elongated and pressurized,[9,10] do not indicate fission after collapse. This is an issue that warrants further examination because accurate prediction of the collapsing process of laser-induced bubbles requires careful accounting of liquid evaporation[11] and compressibility effects during the final stages of collapse.

ACKNOWLEDGMENTS

K.T. also wishes to acknowledge the HRAKLEITOS Program of the Greek Ministry of Education for financial support during this work.

[1] J. W. Strutt (Lord Rayleigh), "On the pressure developed in a liquid during the collapse of a spherical cavity," Philos. Mag. **34**, 94 (1917).
[2] L. Guerri, G. Lucca, and A. Prosperetti, "A numerical method for the dynamics of non-spherical cavitation bubbles," in *Proceedings of the 2nd International Colloquium on Drops and Bubbles*, edited by D. H. LeCroisette (Jet Propulsion Laboratory, Pasadena, CA, 1982) (Publ. 82–7), pp. 175–181.
[3] J. R. Blake, B. B. Taib, and G. Doherty, "Transient cavities near boundaries. Part 1: Rigid boundary," J. Fluid Mech. **170**, 479 (1986).
[4] Y. Tomita and A. Shima, "Mechanisms of impulsive pressure generation and damage pit formation by bubble collapse," J. Fluid Mech. **169**, 535 (1986).
[5] A. Philipp and W. Lauterborn, "Cavitation erosion by single laser-produced bubbles," J. Fluid Mech. **361**, 75 (1998).
[6] A. Pearson, J. R. Blake, and S. R. Otto, "Jets in bubbles," J. Eng. Math. **48**, 391 (2004).
[7] O. Lindau and W. Lauterborn, "Cinematographic observation of the collapse and rebound of a laser-produced cavitation bubble near a wall," J. Fluid Mech. **479**, 327 (2003).
[8] F. D. Gaitan, L. A. Crum, C. C. Church, and R. A. Roy, "Sonoluminescence and bubble dynamics for a single, stable, cavitation bubble," J. Acoust. Soc. Am. **91**, 3166 (1992).
[9] C. D. Ohl, O. Lindau, and W. Lauterborn, "Luminescence from spherically and aspherically collapsing laser bubbles," Phys. Rev. Lett. **80**, 393 (1998).
[10] R. Geisler, "Untersuchungen zur Laserinduzierten Kavitation mit Nanosekunden–Femtosekundenlasern," Ph.D. thesis, University of Goettingen (2004).
[11] B. D. Storey and A. J. Szeri, "Water vapor, sonoluminescence and sonochemistry," Proc. R. Soc. London, Ser. A **456**, 1685 (2000).
[12] S. Hilgenfeldt, D. Lohse, and H. P. Brenner, "Phase diagrams for sonoluminescing bubbles," Phys. Fluids **8**, 2608 (1996); erratum, *ibid.* **9**, 2462 (1996).
[13] J.-K. Choi and G. L. Chahine, "Non-spherical bubble behavior in vortex flow fields," Comput. Mech. **32**, 281 (2003).
[14] J.-K. Choi and G. L. Chahine, "Noise due to extreme bubble deformation near inception of tip vortex cavitation," Phys. Fluids **16**, 2411 (2004).
[15] G. L. Chahine, in *Fluid Vortices*, edited by S. I. Green (Kluwer Academic,

Dordrecht, 1995), Chap. 18, pp. 783–828.
[16] T. B. Benjamin and A. T. Ellis, "The collapse of cavitation bubbles and the pressures thereby produced against solid boundaries," Philos. Trans. R. Soc. London, Ser. A **260**, 221 (1966).
[17] J. R. Blake, M. C. Hooton, P. B. Robinson, and R. P. Tong, "Collapsing cavities, toroidal bubbles and jet impact," Philos. Trans. R. Soc. London, Ser. A **355**, 537 (1997).
[18] J. P. Best, "The formation of toroidal bubbles upon the collapse of transient cavities," J. Fluid Mech. **251**, 79 (1993).
[19] T. S. Lundgren and N. N. Mansour, "Oscillations of drops in zero gravity with weak viscous effects," J. Fluid Mech. **194**, 479 (1988).
[20] K. Tsiglifis and N. Pelekasis, "Nonlinear oscillations and collapse of elongated bubbles subject to weak viscous effects," Phys. Fluids **17**, 102101 (2005).
[21] G. K. Batchelor, *An Introduction to Fluid Dynamics* (Cambridge University Press, Cambridge, UK, 1967).
[22] D. Leppinen and J. R. Lister, "Capillary pinch-off in inviscid liquids," Phys. Fluids **15**, 568 (2003).